

Communication

Time Domain Simulated Characterization of the Coplanar Waveguide in an On-Chip System for Millimeter Waveform Metrology

Kejia Zhao ^{1,*}, He Chen ¹, Xiangjun Li ^{2,*}, Jie Sun ³, Bo Li ¹, Dexian Yan ² and Lanlan Li ¹

¹ National Institute of Metrology, Beijing 100029, China; chenhe@nim.ac.cn (H.C.); libo@nim.ac.cn (B.L.); lill@nim.ac.cn (L.L.)

² Center for THz Research, China Jiliang University, Hangzhou 310018, China; yandexian1991@cjl.edu.cn

³ Zhejiang Institute of Metrology, Hangzhou 310018, China; jiesun1022@163.com

* Correspondence: zhaokj@nim.ac.cn (K.Z.); xiangjun_li@cjl.edu.cn (X.L.)

Abstract: We investigate the time domain characterization of a coplanar waveguide (CPW) based on an on-chip electro-optic sampling (EOS) system for millimeter waveform metrology. The CPW is fabricated on a thin layer of low-temperature gallium arsenide (LT-GaAs), and the substrate material is GaAs. A femtosecond laser generates and detects ultrashort pulses on the CPW. The forward propagating pulses are simulated using a simplified current source for the femtosecond laser at different positions on the CPW for the first time. Then, the influences of the CPW geometry parameters on the measured pulses are discussed. The varying slot width has larger influences on the amplitude of millimeter wave pulses than the center conductor width and the pumping gap. Finally, in the frequency range of 10 GHz to 500 GHz, the transfer functions calculated by the time domain pulses are in good agreement with the transfer functions calculated by the frequency domain ports. The above results are important for improving the measurement precision of the millimeter waveform on the CPW for millimeter waveform metrology.

Keywords: coplanar waveguide; electro-optic sampling; millimeter wave; waveform metrology



Citation: Zhao, K.; Chen, H.; Li, X.; Sun, J.; Li, B.; Yan, D.; Li, L. Time Domain Simulated Characterization of the Coplanar Waveguide in an On-Chip System for Millimeter Waveform Metrology. *Electronics* **2024**, *13*, 145. <https://doi.org/10.3390/electronics13010145>

Academic Editor: Reza K. Amineh

Received: 14 October 2023

Revised: 18 December 2023

Accepted: 22 December 2023

Published: 28 December 2023



Copyright: © 2023 by the authors. Licensee MDPI, Basel, Switzerland. This article is an open access article distributed under the terms and conditions of the Creative Commons Attribution (CC BY) license (<https://creativecommons.org/licenses/by/4.0/>).

1. Introduction

Currently, the millimeter wave (60 GHz~300 GHz) is increasingly utilized in several key applications, such as high-speed communications, non-destructive sensing, spectroscopy, and imaging [1–5]. Ultrafast switching and extremely high-frequency operation are key issues for these applications. However, there are great challenges in the uniform measurements of ultrashort pulse generators in the millimeter wave range based on electronic components in ultra-wideband oscilloscopes and related technology [6]. Fortunately, an alternative approach was found based on the electro-optic sampling (EOS) principle compared to traditional sampling oscilloscopes with a bandwidth smaller than 50 GHz [7,8]. Using femtosecond laser pulses as the sampling pulses, EOS technology can extend its working bandwidths into the terahertz range. It allows the simultaneous measurement of the amplitude and phase of the millimeter wave or the THz pulse electric field in the time domain, with subsequent Fourier transform providing spectral characteristics in the 0.1~30 THz frequency range [9]. EOS for measuring the parameters of ultrashort electrical pulses has been verified as a promising method of full waveform metrology since 2001 [10]. In 2018~2019, the first international comparisons of the initial EOS apparatus operated by the National Institute of Standards and Technology (NIST), the Physikalisch-Technische Bundesanstalt (PTB), and the National Institute of Metrology (NIM) were conducted using a bandwidth of more than 110 GHz [11]. At present, pulses with a bandwidth of more than 10 THz can be measured using the EOS system [12–16].

The core part of the popular EOS system for millimeter waveform metrology is a combination of a coplanar waveguide (CPW) and a photoconductive structure [8,17]. The time domain measurement of the voltage pulses can be carried out at different positions along the waveguide, which makes it possible to separate voltage pulses propagating in forward and backward directions. By using digital signal-processing algorithms, those temporally overlapped waveforms will be divided completely. This separation method is equivalent to using directional flexible couplers in VNAs, which constitutes the main advances of the EOS system in millimeter waveform metrology. At present, the time domain measurement is able to generate an epoch of over 2 ns corresponding to a frequency spacing of 500 MHz, and the usable bandwidth of the voltage pulses extends up to 500 GHz [17]. Another advantage of this configuration is that the same laser source is applied to generate and detect the ultrashort voltage pulses in the same substrate, which significantly simplifies the experimental setup and reduces the uncertainty of electro-optic (EO) measurements. However, this kind of EOS measurement demands good characterization of the on-wafer coplanar waveguide and de-embedding of the probe [6–8]. Additionally, the voltage pulses must be transferred from the CPW to a coaxial waveguide of the device under test. Though there are many experimental results [8,17], the propagation mechanism of pulses along the CPW is still unclear and should be further investigated by full electromagnetic wave simulation tools, such as the Finite Element Method (FEM) or the Finite Difference Time domain (FDTD).

In this paper, we investigate the time domain characterization of the CPW based on an on-chip EOS system for millimeter waveform metrology. However, if we simulate the whole generating and detecting procedure of the pulse waveform, including optical, millimeter electromagnetic waves and the time-dependent carrier dynamics, in the semiconductor simulation, the computational cost is usually huge and needs a very long time [18]. To improve the research efficiency, the millimeter wave pulse generation process can be simplified by introducing a current source that is equivalent to the laser pulse excitation [19]. Here, we characterize the CPW using both the time domain and the frequency domain simulations. The CPW is fabricated on a thin layer of low-temperature gallium arsenide (LT-GaAs) using a GaAs substrate. For the first time, we simulate the forward propagating pulses at different positions on the CPW by simplifying the excitation of a laser pulse as a current source, which enables the highly efficient characterization of the EOS system before and after the experiments. Meanwhile, the influence of several CPW geometry parameters on the measured pulses is well discussed by characteristic impedance in the circuit theory and fast Fourier translation. Finally, the transfer functions of the CPW with different lengths are calculated by the pulses at different positions. There is good consistency between the results from a transformation of the time domain pulses and direct simulations from the frequency domain. The undergoing propagation rules of pulses along the CPW are useful for the future realization of EOS for millimeter waveform metrology.

2. Design Scheme and Research Method

The on-chip system based on EOS technology for millimeter waveform metrology is schematically demonstrated in Figure 1. The ultrashort pulses are produced by focusing the femtosecond laser beam with an 800 nm center wavelength (referred to as the pump beam) onto a biased photoconductive gap on the center conductor of a 2-mm-long CPW. The full width at half maximum (FWHM) of the optical pulses is about 100 fs as generated from an autocorrelation. Figure 1 shows the conventional CPW structure with signal and ground lines on a GaAs substrate. The fundamental dimensional parameters are the real permittivity of GaAs $\epsilon_{\text{GaAs}} = 12.7$, the signal width $w = 45 \mu\text{m}$, the air slot width $s = 30 \mu\text{m}$, the gold thickness $t_m = 0.5 \mu\text{m}$, the LT-GaAs thickness $t_{d1} = 1 \mu\text{m}$, and the GaAs thickness $t_{d2} = 200 \mu\text{m}$. For full-wave electromagnetic (EM) analysis, the structure is enclosed in a box with perfect match layer (PML) boundaries. At the left edge of the CPW, a photoconductive structure as a gap $g = 10 \mu\text{m}$ is integrated into the center conductor, which is biased by a 25 V voltage source. The waveguide has been fabricated on a 1-micrometer-thick layer

of LT-GaAs with a shorter carrier lifetime, causing the optically induced conductivity to quickly vanish in the photoconductive gap. The main advantage of the structure is that one laser source can completely generate and detect ultrashort pulses in the same material without external EO probes [20]. This on-chip system significantly simplifies the experimental setup and reduces the uncertainty of EOS measurements for millimeter waveform metrology [6].

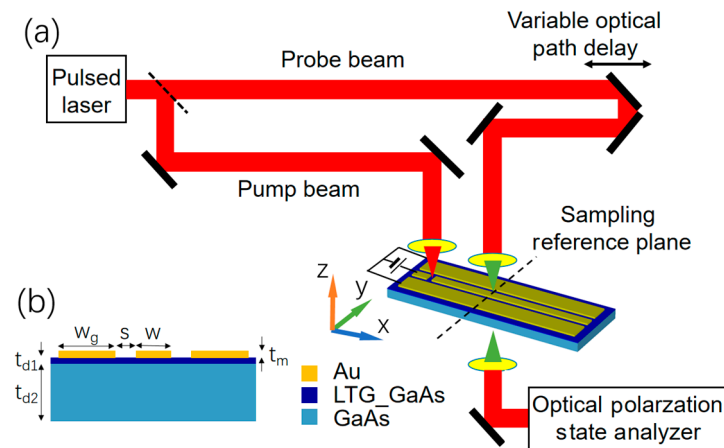


Figure 1. (a) The system diagram. (b) Cross-section of the CPW, $\epsilon_{GaAs} = 12.7$, $w = 45 \mu\text{m}$, $w_g = 500 \mu\text{m}$, $s = 30 \mu\text{m}$, $t_m = 0.5 \mu\text{m}$, $t_{d1} = 1 \mu\text{m}$, $t_{d2} = 200 \mu\text{m}$. For full-wave electromagnetic analysis, the structure is enclosed in a box with the PML boundaries.

It is known that the electrical response of the gap to the carriers generated from the femtosecond laser excitation and their acceleration with a bias voltage at the electrodes is dominated by the coupled Poisson's and drift–diffusion equations for the semiconductor [18]. By solving the time and spatial-dependent electric potential and the carrier concentration, we can obtain a time-dependent photocurrent current density accounting for the femtosecond laser Gaussian envelope, which leads to the millimeter wave pulse emerging and propagating along the CPW. However, the computational cost is usually huge and needs a long time if the whole generating or detecting procedure of the voltage pulse is simulated. The complex calculation includes optical and millimeter electromagnetic wave propagation, the time-dependent carrier dynamics in the semiconductor, and their coupling procedure.

To simplify the simulating characteristics of the CPW in the on-chip system, we intend not to perform the whole calculation including the electrical response of the gap to the carriers generated from the femtosecond laser excitation. Here, we use a current source instead of directly calculating the response of the LT-GaAs to the optical femtosecond laser pulse. This laser excites a current on the gap of the center conductor represented as a current source in the simulation as shown in Figure 2a. There is also a two-port network model for the CPW in the underpart of Figure 2a. This allows us to fully describe the electrical transmissions and reflections of high-frequency devices, including a full mismatch correction. The mismatch happens when the independence of the CPW is different from the coaxial waveguide of the device under test. The current induced by the laser can be imported to commercial FEM software (version HFSS 18.1) named High-Frequency Simulator Structure (HFSS) from the former simulation results of the optical femtosecond laser pulse on the LT-GaAs [18], as illustrated in Figure 2b. With careful consideration, our investigating strategy is to use a custom monitor to obtain the average electric field on the spots of the probing laser, which represents the millimeter waveform we measured in the experiment.

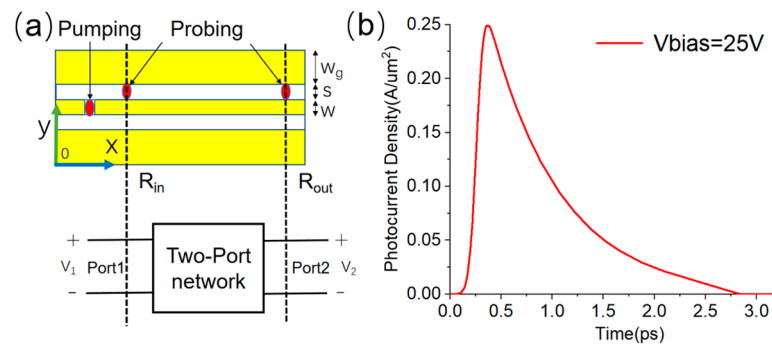


Figure 2. (a) The pumping and probing laser spots at different reference planes on the CPW and the two-port model based on the circuit theory. (b) Photocurrent density produced by Gauss shape pumping laser beam.

Theoretically, the voltage pulses generated by the laser pumping at the gap propagate along the CPW at both the $+x$ and $-x$ directions. Here, if we assume that the ports absorb all the incoming electromagnetic waves, there will be no reflections from the ports. We can obtain the waveform at different positions of the CPW by simulation. The transfer functions of the CPW can be taken by Fourier transformations of waveforms in the time domain or by ports in the frequency domain directly.

In the following part, we demonstrate the details of the forward propagating pulses at different positions on the CPW as well as the influence of the CPW geometry parameters. Finally, the transfer functions of the CPW with different lengths are calculated by the pulses at different positions.

3. Simulation Results and Discussion

Firstly, we discuss the influence of the center conductor width and slot width on the real part of the characteristic impedance $\text{Re}(Z_c)$ and the reflection coefficient amplitude $|S_{11}|$ of the CPW ranging from 10 GHz~500 GHz. The characteristic impedance of the CPW should be 50Ω to match the outer circuits and the probes of the vector network analyzer. Figure 3a,c show the simulation results of the real part of the characteristic impedance using the analytic model [21], and Figure 3b,d demonstrate the reflection coefficient by the FEM method for the 2-mm-long CPW without the gap. The slot width s changes from $30 \mu\text{m}$ to $60 \mu\text{m}$ with $w = 45 \mu\text{m}$ for Figure 3b. The center conductor width w varies from $30 \mu\text{m}$ to $60 \mu\text{m}$ with $s = 30 \mu\text{m}$ for Figure 3c,d. The $\text{Re}(Z_c)$ increases as the w increases and approaches approximately 50Ω when the w is about $40\sim 45 \mu\text{m}$ within the frequency range of 10 GHz to 500 GHz. The $\text{Re}(Z_c)$ decreases as the s increases, and it approaches approximately 50Ω when the s is about $30\sim 35 \mu\text{m}$ within the same frequency band. The $|S_{11}|$ approaches zero when the $\text{Re}(Z_c)$ is close to 50Ω . The $\text{Re}(Z_c)$ cannot be kept at 50Ω at each frequency at the same time. In the entire working frequency range, it should be ensured that the deviation between the $\text{Re}(Z_c)$ and 50Ω at the center frequency is the smallest. Here, we choose the values of $w = 45 \mu\text{m}$ and $s = 30 \mu\text{m}$ because in this case, the $\text{Re}(Z_c)$ is very close to 50Ω at 250 GHz. The ripples presented in Figure 3b,d illustrate that when the geometry of the CPW is fixed, the reflection spectra have peaks and valleys as the frequency varies. The reason for this phenomenon should be attributed to the characteristic impedance increases and decreases in a broad frequency scope. At the same time, the group delay is closely related to the characteristic impedance feature in the wide frequency domain, though the results are based on the frequency domain simulation, which can be indirectly measured by the EOS system. Our direct simulations of the waveforms are important to validate the measurement results in the experiment for these characteristic impedance features.

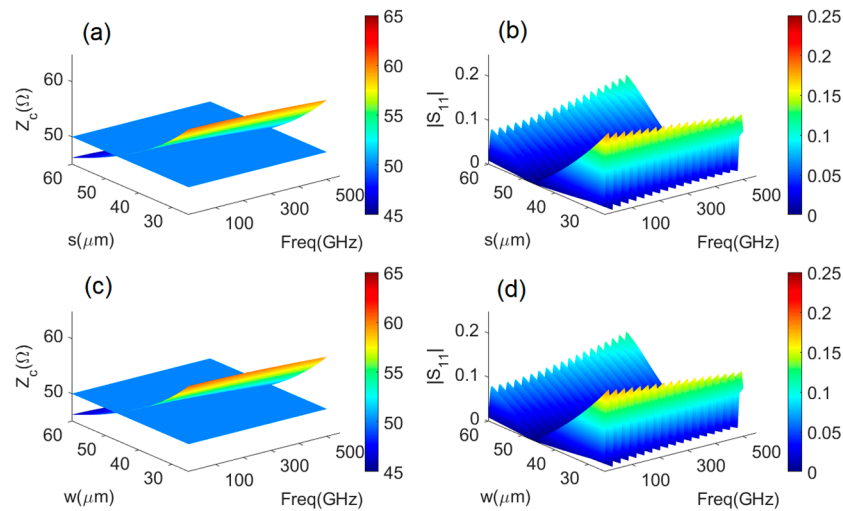


Figure 3. Simulation results of (a,c) characteristic impedance real parts and (b,d) reflection $|S_{11}|$ vary as slot width $s = 30\sim 60\ \mu\text{m}$ ($w = 45\ \mu\text{m}$) and center conductor width $w = 30\sim 60\ \mu\text{m}$ ($s = 30\ \mu\text{m}$) with the frequency ranging from 10 GHz to 500 GHz.

Secondly, we explore the voltage pulses, which can be detected by the probing laser when the geometry parameters of the CPW change. The response of the LT-GaAs on the gap to the optical femtosecond laser pulse is replaced by a current source instead of directly calculating the whole photoconductive effect. The current data are imported to HFSS, and after simulation, the integrated electric field on the spots of the probing laser is obtained. Figure 4a shows the pulse profiles at different detecting positions with $x = 500\ \mu\text{m}$, $1000\ \mu\text{m}$, $1500\ \mu\text{m}$, and $2000\ \mu\text{m}$, with the gap at $x = 250\ \mu\text{m}$. It is noted that the amplitudes of the pulses gradually decrease with an increase in the detecting distance, and the FWHM gradually increases from 1.4 ps to 2.6 ps. Furthermore, for the probing at $x = 2000\ \mu\text{m}$, the influences of w , s , and g on the pulses has also been investigated. Figure 4b demonstrates the pulses with $s = 20\ \mu\text{m}$, $25\ \mu\text{m}$, $30\ \mu\text{m}$, and $35\ \mu\text{m}$. The amplitudes of the pulses gradually decrease with an increase in the s , and the FWHM also gradually increases. Figure 4c illustrates the pulses with $w = 45\ \mu\text{m}$, $50\ \mu\text{m}$, $55\ \mu\text{m}$, and $60\ \mu\text{m}$. The amplitudes of the pulses gradually decrease with an increase in the w , and the FWHM also gradually increases at the same. Figure 4d shows the pulses with the $g = 5\ \mu\text{m}$, $10\ \mu\text{m}$, $15\ \mu\text{m}$, and $20\ \mu\text{m}$. The amplitudes of the pulses gradually increase with the augmentation of g , but the FWHM gradually decreases. Correspondingly, we also calculate the fast Fourier transform (FFT) of the pulses for the above-mentioned varying parameters, as depicted in Figure 5. As the width of the pulse in the time domain becomes wider, its frequency band becomes narrower. All the parameters influence the shapes of the voltage pulses, and the revealed trends are important for the EOS on-chip system design.

In order to reveal the impact of the geometry parameters of the CPW on the probed voltage pulses, a lump port is applied to the laser pumping gap, and the electrical field intensity distributions of the CPW at 100 GHz are demonstrated. Figure 6 illustrates the intensity distributions on the xy plane with $z = 0\ \text{mm}$, the yz plane with $x = 1\ \text{mm}$, and the yz plane with $x = 0.25\ \text{mm}$ (the center of the laser pumping gap). It is evident that the majority of the electrical field energy is distributed at two slots of the CPW. Furthermore, the energy is focused at the edges of slots, particularly on the sides of the center conductor, as shown in Figure 6b. Therefore, the varying of the slot width s has a greater impact on the amplitude of the millimeter wave pulses compared to the center conductor width w and the pumping gap g . The area of the electrical field intensity in the pumping gap g is smaller, resulting in a weaker effect on the pulse amplitude.

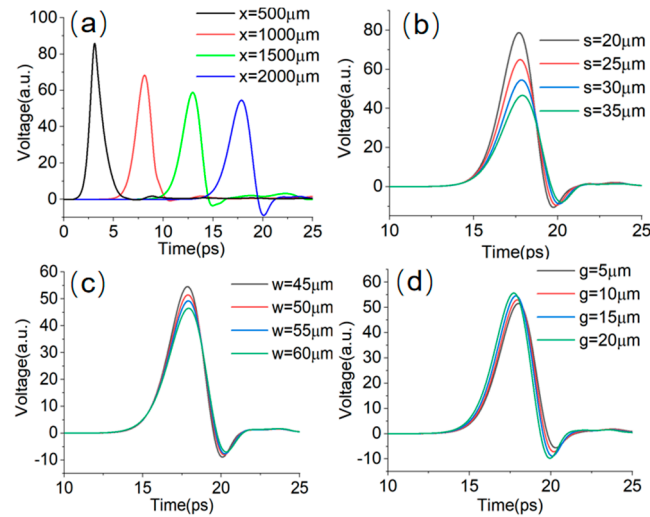


Figure 4. The pulses varying with (a) the position x , (b) the slot width s , (c) the center conductor width w , and (d) the pumping gap g with laser probing at $x = 2000 \mu\text{m}$.

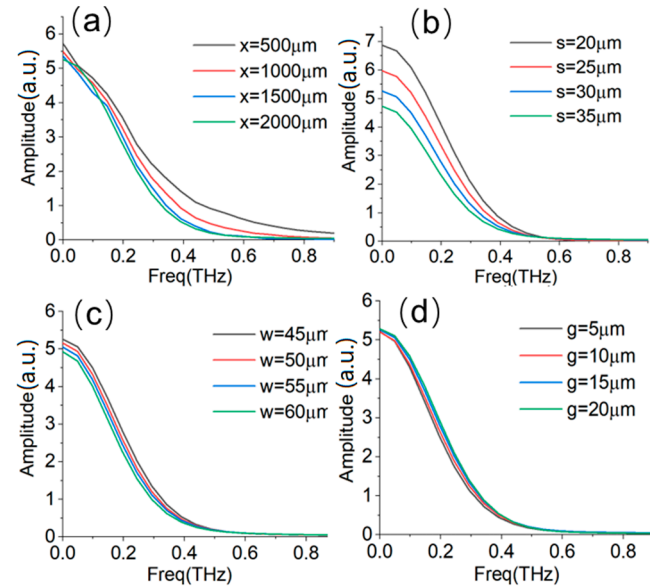


Figure 5. The FFTs of pulses varying with (a) the position x , (b) the slot width s , (c) the center conductor width w , and (d) the pumping gap g with laser probing at $x = 2000 \mu\text{m}$.

In the next step, we discuss how to obtain the transfer functions of the CPW from the pulses calculated at the different positions along the slot of the CPW, as shown in the following equation:

$$H(\omega) = \frac{V_{out}(\omega)}{V_{in}(\omega)} = \frac{FFT(v_{out}(t))}{FFT(v_{in}(t))} \quad (1)$$

where FFT indicates the operation of the fast Fourier transform. The time domain pulses can be measured by the EOS system in Figure 1. The transfer functions of the CPW can be acquired by Equation (1). The precise models of the CPW are very important in reducing the uncertainty of the EOS measurements for millimeter waveform metrology.

Figure 7 shows the pulse profiles and the transmission coefficients $|S_{21}|$ calculated from Equation (1) by inputting the pulse at $x = 500 \mu\text{m}$ and detecting the output pulses at $x = 1000 \mu\text{m}$, $1500 \mu\text{m}$, and $2000 \mu\text{m}$. The corresponding lengths of the CPW are $L = 500 \mu\text{m}$, $1000 \mu\text{m}$, and $1500 \mu\text{m}$ in the red, green, and blue colors. Those results are compared with the direction FEM calculation results of the frequency domain by a two-port model with the same lengths in Figure 6b. There is good consistency between the results from the two

different methods from the time domain and frequency domain. The time domain pulses can be directly taken from the measurement results from the EOS system. This allows us to characterize the high-frequency devices with a full mismatch correction by numerically rebuilding the measured waveform with an accurate transfer function of the CPW.

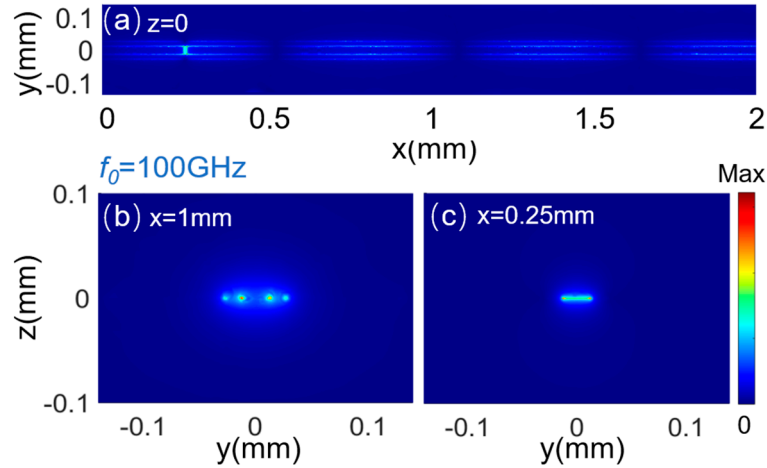


Figure 6. Electrical field intensity distributions of CPW at 100 GHz, (a) the yox plane with $z = 0$ mm, (b) the yoz plane with $x = 1$ mm, and (c) the yoz plane with $x = 0.25$ mm (the laser pumping gap center).

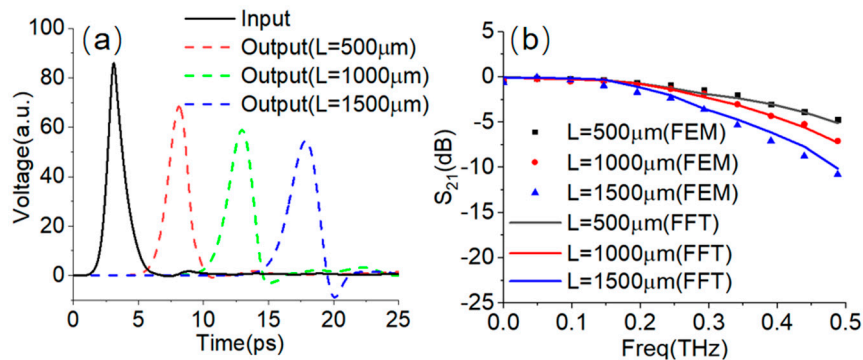


Figure 7. (a) The pulses as input and outputs with $L = 500 \mu\text{m}$, $1000 \mu\text{m}$, and $1500 \mu\text{m}$, (b) transmission coefficient of the CPW with pulses at different L , simulated by ports (dots) and calculated by pulses (solid lines).

4. Conclusions

In this work, based on the EOS system, an on-chip system is designed for millimeter waveform metrology with a CPW structure. The CPW is patterned on a thin layer of LT-GaAs using a GaAs substrate. The generation and detection of ultrashort pulses are realized on the CPW using one femtosecond laser. The forward propagating pulses are simulated at different positions on the CPW using a simplified current source instead of directly calculating the entire photoconductive effect. With digital signal-processing algorithms, even those temporally overlapping waveforms can be separated completely with proper known conditions. Additionally, the influence of the CPW geometry parameters on the measured pulses is discussed. The varying of the slot width has a greater influence on the amplitude of the millimeter wave pulses compared to the center conductor width and the pumping gap. This is due to the concentration of the electrical field intensity primarily occurring at the two slots of the CPW. Finally, the transfer functions of the CPW in the frequency range of 10~500 GHz with different lengths are calculated by the pulses at different positions. There is good consistency between the time domain pulse results and the direct simulations from the frequency domain with a two-port model. The above

results are important for the precision measurements of the millimeter waveform and the realization of a voltage pulse standard.

Author Contributions: Conceptualization, K.Z. and X.L.; methodology, H.C. and X.L.; software, X.L.; validation, J.S. and B.L.; resources, L.L.; writing—original draft preparation, K.Z. and X.L.; writing—review and editing, D.Y.; funding acquisition, K.Z. and X.L. All authors have read and agreed to the published version of the manuscript.

Funding: This work was supported by the National Quality Infrastructure System (No. 2022YFF0605902).

Data Availability Statement: The data can be shared upon request.

Conflicts of Interest: The authors declare no conflict of interest.

References

- Hong, W.; Jiang, Z.H.; Yu, C.; Hou, D.; Wang, H.; Guo, C.; Hu, Y.; Kuai, L.; Yu, Y.; Jiang, Z.; et al. The Role of Millimeter-Wave Technologies in 5G/6G Wireless Communications. *IEEE J. Microw.* **2021**, *1*, 101–122. [[CrossRef](#)]
- Wang, X.; Kong, L.; Kong, F.; Qiu, F.; Xia, M.; Arnon, S.; Chen, G. Millimeter Wave Communication: A Comprehensive Survey. *IEEE Commun. Surv. Tutor.* **2018**, *20*, 1616–1653. [[CrossRef](#)]
- van Berlo, B.; Elkelany, A.; Ozecebi, T.; Meratnia, N. Millimeter Wave Sensing: A Review of Application Pipelines and Building Blocks. *IEEE Sens. J.* **2021**, *21*, 10332–10368. [[CrossRef](#)]
- Wang, Z.; Chang, T.; Cui, H.-L. Review of Active Millimeter Wave Imaging Techniques for Personnel Security Screening. *IEEE Access* **2019**, *7*, 148336–148350. [[CrossRef](#)]
- Rothbart, N.; Holz, O.; Koczulla, R.; Schmalz, K.; Hübers, H.-W. Analysis of Human Breath by Millimeter-Wave/Terahertz Spectroscopy. *Sensors* **2019**, *19*, 2719. [[CrossRef](#)] [[PubMed](#)]
- Bieler, M.; Spitzer, M.; Pierz, K.; Siegner, U. Improved Optoelectronic Technique for the Time-Domain Characterization of Sampling Oscilloscopes. *IEEE Trans. Instrum. Meas.* **2008**, *58*, 1065–1071. [[CrossRef](#)]
- Struszewski, P.; Pierz, K.; Bieler, M. Time-Domain Characterization of High-Speed Photodetectors. *J. Infrared Millimeter Terahertz Waves* **2017**, *38*, 1416–1431. [[CrossRef](#)]
- Struszewski, P.; Bieler, M. Asynchronous optical sampling for laser-based vector network analysis on coplanar waveguides. *IEEE Trans. Instrum. Meas.* **2019**, *68*, 2295–2302. [[CrossRef](#)]
- Li, E.; Yang, J.; Zhang, K.; Li, H.; Xu, Y.; Su, F.; Wang, T.; Fang, G. Systematic Study of Two-Color Air Plasma Broadband THz-TDS. *IEEE Trans. Terahertz Sci. Technol.* **2023**, *13*, 476–484. [[CrossRef](#)]
- Williams, D.F.; Hale, P.D.; Clement, T.S.; Morgan, J.M. Calibrating electro-optic sampling systems. In Proceedings of the in 2001 IEEE MTT-S International Microwave Symposium Digest (Cat. No. 01CH37157), Phoenix, AZ, USA, 20–24 May 2001; Volume 3, pp. 1527–1530.
- Bieler, M.; Struszewski, P.; Feldman, A.; Jargon, J.; Hale, P.; Gong, P.; Xie, W.; Yang, C.; Feng, Z.; Zhao, K.; et al. International comparison on ultrafast waveform metrology. In Proceedings of the in 2020 Conference on Precision Electromagnetic Measurements (CPEM), Denver, CO, USA, 24–28 August 2020.
- Karpowicz, N.; Dai, J.; Lu, X.; Chen, Y.; Yamaguchi, M.; Zhao, H.; Zhang, X.-C.; Zhang, L.; Zhang, C.; Price-Gallagher, M. Coherent heterodyne time-domain spectrometry covering the entire “terahertz gap”. *Appl. Phys. Lett.* **2008**, *92*, 011131. [[CrossRef](#)]
- Feng, Z.; Zhao, K.; Yang, Z.; Miao, J.; Chen, H. 100 GHz pulse waveform measurement based on electro-optic sampling. *Laser Phys.* **2018**, *28*, 055301. [[CrossRef](#)]
- Feng, Z.; Zhao, K.; Li, B.; Yang, Z.; Song, Z.; Cui, X. Pulse waveform characterization by electro-optic sampling at NIM. In Proceedings of the in 2020 Conference on Precision Electromagnetic Measurements (CPEM), Denver, CO, USA, 24–28 August 2020; pp. 1–2.
- Han, C.; Wang, Y.; Li, Y.; Chen, Y.; Abbasi, N.A.; Kurner, T.F.; Molisch, A. Terahertz Wireless Channels: A Holistic Survey on Measurement, Modeling, and Analysis. *IEEE Commun. Surv. Tutor.* **2022**, *24*, 1670–1707. [[CrossRef](#)]
- Chen, H.; Zhao, K.J.; Li, X.J.; Li, B.; Li, L. Bandwidth Improvement of Coplanar Waveguide for Electro-optic Sampling System. In Proceedings of the 2022 International Conference on Microwave and Millimeter Wave Technology (ICMMT), Harbin, China, 12–15 August 2022; pp. 1–3.
- Bieler, M.; Fuser, H.; Pierz, K. Time-Domain Optoelectronic Vector Network Analysis on Coplanar Waveguides. *IEEE Trans. Microw. Theory Tech.* **2015**, *63*, 3775–3784. [[CrossRef](#)]
- Burford, N.; El-Shenawee, M. Computational modeling of plasmonic thin-film terahertz photoconductive antennas. *J. Opt. Soc. Am. B* **2016**, *33*, 748–759. [[CrossRef](#)]
- Nguyen, T.K.; Kim, W.T.; Kang, B.J.; Bark, H.S.; Kim, K.; Lee, J.; Park, I.; Jeon, T.-I.; Rotermund, F. Photoconductive dipole antennas for efficient terahertz receiver. *Opt. Commun.* **2016**, *383*, 50–56. [[CrossRef](#)]

20. Bieler, M.; Spitzer, M.; Hein, G.; Siegner, U. Time-domain characterisation of non-coplanar high-frequency components up to 300 GHz. *Electron. Lett.* **2002**, *38*, 1038–1039. [[CrossRef](#)]
21. Heinrich, W. Quasi-TEM description of MMIC coplanar lines including conductor-loss effects. *IEEE Trans. Microw. Theory Tech.* **1993**, *41*, 45–52. [[CrossRef](#)]

Disclaimer/Publisher’s Note: The statements, opinions and data contained in all publications are solely those of the individual author(s) and contributor(s) and not of MDPI and/or the editor(s). MDPI and/or the editor(s) disclaim responsibility for any injury to people or property resulting from any ideas, methods, instructions or products referred to in the content.